Three-dimensional hierarchical porous TiO$_2$/graphene aerogels as promising anchoring materials for lithium–sulfur batteries

Jia Wang, Cuimei Fu, Xiaofei Wang, Yimin Yao, Minglin Sun, Lina Wang[*], Tianxi Liu[**]

State Key Laboratory for Modification of Chemical Fibers and Polymer Materials, College of Materials Science and Engineering, Innovation Center for Textile Science and Technology, Donghua University, Shanghai 201620, China

ARTICLE INFO

ABSTRACT

The main obstacle for broad adaption of lithium−sulfur (Li−S) batteries originates from the shuttle effect of electrolyte-soluble intermediates of lithium polysulfides (Li$_2$S$_n$, $4 \leq n \leq 8$). Rational design of multifunctional sulfur cathodes with porous conductive matrix and large polar sites is greatly desired. Herein, we report three-dimensional hierarchical porous TiO$_2$/graphene aerogel (TiO$_2$/GA) composites as promising anchoring materials for sulfur species. Various TiO$_2$/GA composites with 3.5, 15.3, 54.6 and 75.2 wt% TiO$_2$ are synthesized via a one-pot hydrothermal process. Specifically, the one containing 15.3 wt% TiO$_2$ exhibits a superior boost in specific capacity, rate capability and cyclability. The factors contribute to the high performance attributing much to the strong interfacial chemical and physical interactions of TiO$_2$/GA with Li$_2$S$_n$. Moreover, further improved sulfur utilization is achieved by adding glucose to adjust the surface area and pore size distribution of the aerogels. At a high rate of 2 C (1 C = 1675 mA g^{-1}), an initial discharge capacity up to 1011 mAh g^{-1} is obtained with a decent cyclic efficiency and 100% coulombic efficiency over 500 cycles. These results bring a broad perspective for the future design on practical sulfur-based electrodes.

© 2018 Elsevier Ltd. All rights reserved.

1. Introduction

With the rapid development of new energy technologies, lithium-ion (Li-ion) batteries have been the major energy supply devices for almost all of the current electric vehicles and portable electronic devices. However, the energy density of Li-ion batteries based on the transition metal intercalation compounds (LiCoO$_2$, LiMn$_2$O$_4$, LiFePO$_4$, etc.) [1−3] cannot meet the demands of long-life capacity development. Lithium–sulfur (Li–S) batteries are regarded as the most promising candidates for the next–generation energy storage systems owing to their ultrahigh theoretical discharge capacity (1675 mAh g^{-1}) and energy density (2576 Wh kg^{-1}) [4,5]. However, the commercial development and application of Li–S batteries have been hindered by the intrinsic insulation of elemental sulfur (S$_8$, 5×10^{-30} S cm^{-1}) and its reductive product of lithium sulfide (Li$_2$S, 10^{-13} S cm^{-1}), large volume expansion (about 80% from S$_8$ to Li$_2$S), and especially the soluble intermediate products of lithium polysulfides (Li$_2$S$_n$, $4 \leq n \leq 8$). Unstable sulfur cathode can cause the internal shutting of the dissolved Li$_2$S$_n$ between cathode and lithium anode during the charge and discharge processes [6−10]. This shuttle effect leads to insufficient specific capacity, poor cyclic performance and low coulombic efficiency of the batteries [11,12].

Carbon is highly effective as an electronic conduit, and it can also act as a framework to encapsulate the redox products of sulfur [4]. In order to address the obstacles of Li–S batteries, a straightforward solution is the synthesis and modification of conductive hosts of carbon materials, including micro/mesoporous carbon [13,14], hollow carbon spheres [15], carbon nanofibers [16,17], carbon nanotubes [18,19], graphene nanosheets [20], and so on. In spite of highly improved conductivity of cathodes has been realized, the nonpolar surface of carbon has poor affinity for the polar polysulfides, which cannot effectively block the shuttle effect [21]. Polar materials are thought to form relatively strong chemical bonds with Li$_2$S$_n$ [22,23]. It has been reported that many polar host materials, such as MnO$_2$ [24,25], TiO$_2$ [26−28], V$_2$O$_5$ [29,30], etc., can effectively trap soluble polysulfides on the basis of the interactions between polar molecules [31]. In particular, TiO$_2$ has been proven to be particularly promising for application in Li–S battery cathode materials due to its excellent adsorption ability,

* Corresponding author.
** Corresponding author.
 E-mail addresses: linawang@dhu.edu.cn (L. Wang), txliu@dhu.edu.cn (T. Liu).

non-toxic and favorable cost [32–34]. Sulfur–TiO$_2$ yolk–shell nanoarchitecture has been reported, which exhibits high capacity retention owing to the effectiveness of the intact TiO$_2$ shell in limiting polysulfide dissolution and diffusion [35]. Graphene aerogels, consisting of three-dimensional interconnected mesoporous and microporous structures, have unique advantages as sulfur hosts due to their lightweight, large specific surface area, superior mechanical elasticity and high conductivity [36,37]. The facile combination and rational structure regulation of TiO$_2$ and graphene aerogels for effectively immobilizing soluble polysulfides is potentially a new way to produce multifunctional cathodes of Li–S batteries.

Herein, we report a rational design and fabrication of light-weight three-dimensional (3D) hierarchical porous TiO$_2$/graphene aerogel (TiO$_2$/GA) composites, which have multifunctional advantages when used as substrates for sulfur electrodes. Firstly, the TiO$_2$/GA network acts as the electrochemical reaction chamber, not only providing some degree of physical entrapment for poly-sulfides, but also accommodating the sulfur volume expansion upon phase transformation during the charge–discharge processes. Secondly, the porous TiO$_2$/GA serves as 3D interconnected conductive matrix, which greatly reduces the resistance of electron and ion transport, thus achieving high rate capabilities. More importantly, ultrafine TiO$_2$ particles are uniformly dispersed on graphene nanosheets, affording abundant chemical adsorption sites for Li$_2$S$_n$ and promoting stable redox activity over the whole lifetime of the cathode material. However, such a unique structure of the interconnected 3D porous network is strongly dependent on the ratios of TiO$_2$ and graphene. Remarkably, the addition of glucose to the precursor can adjust the surface area and pore size contribution of the TiO$_2$/GA composites furthermore, leading to enhanced adsorption of Li$_2$S$_n$. The elaborate cathode delivers an improved electrochemical performance in terms of specific capacity, cyclic stability and rate capability. An initial discharge capacity of 1273, 1178, 1039 and 1011 mAh g^{-1} is obtained at 0.2, 0.5, 1, and 2 C, respectively. And more than 50% of the capacity can be held even after 500 cycles.

2. Experimental section

2.1. Preparation of TiO$_2$/GA composites

In a typical synthetic procedure, graphene oxide (GO, C6G6 Technology Co., Ltd.) was dispersed in water by sonication to 2 mg mL^{-1}. Meanwhile, 100 μL Ti(OC$_4$H$_9$)$_4$ (≥97.0%, SIGMA-ALDRICH) was mixed in 6 mL alcohol to prepare 0.05 M Ti(OC$_4$H$_9$)$_4$-ethanol solution. Then, 500 μL of the solution was dropwise added to 10 mL of GO dispersion under consecutive stirring at the room temperature of 25 °C for 3 h. Subsequently, the obtained solution was transferred into a 50 mL teflon-lined autoclave and maintained at 180 °C for 12 h. After washing with deionized water thoroughly, the obtained TiO$_2$/graphene hydrogel was freeze-dried for 24 h to obtain TiO$_2$/graphene aerogel-1 (TiO$_2$/GA-1) composite. The TiO$_2$/graphene aerogel-2 (TiO$_2$/GA-2) composite was prepared via the same route, except 20 mg glucose was added into the precursor as a crosslinker and dispersing agent. Meanwhile, we prepared other samples with different amount of TiO$_2$ by adding different concentration of Ti(OC$_4$H$_9$)$_4$-ethanol solution (0.01, 0.1 and 0.2 M) into GO dispersions. For a control experiment, pure graphene aerogel (GA) was also prepared by the same method. Pure anatase TiO$_2$ was synthesized by stirring the precursor titanate at room temperature for 3 h, hydrothermal treating at 180 °C for 12 h, centrifuging and vacuum drying overnight at 50 °C.

2.2. Preparation of Li$_2$S$_6$ solution

The Li$_2$S$_6$ solution was prepared by mixing sulfur and Li$_2$S at a molar ratio of 5:1 for S/Li$_2$S in the solvent of 1,3-dioxolane/1,2-dimethoxyethane (DOL/DME, 1:1, v/v) in an Ar-filled glove box.

2.3. Material characterizations

The crystal structure and phase analysis of the products were detected by X-ray diffractometer (D/max-2550VB+/PC, Rigalcu) equipped with Cu-Kα radiation at a scan rate of 4°/min. Raman spectra were detected by an inVia Reflex Raman Spectrometer (inVia-Reflex, Renishaw). Fourier transform infrared spectra (FT-IR) were recorded on a FT-IR spectrometer (Bruker VECTOR22). The morphology and microstructure of the samples were observed by field-emission scanning electron microscopy (FE-SEM, S-4800, HITACHI) and high-resolution transmission electron microscopy (TEM, JEM-2100F, JEOL). The contents of TiO$_2$ in the TiO$_2$/GA composites were examined by thermogravimetry (TG, STA449F5 NETZSCH) analysis in the temperature range of 25–800 °C in air. A Quadrasorb adsorption instrument (Quantachrome Instruments) was used to perform nitrogen sorption/desorption measurements. Meanwhile, the specific surface area was calculated with the multi-point Brunauer–Emmett–Teller (BET) method. The pore size distributions were calculated from nitrogen sorption data using the nonlocal density functional theory (NLDFT) equilibrium model method for slit pores provided by Quantachrome data reduction software ASiQwin Version 4.01. The UV–vis adsorption spectroscopy was performed on polysulfide solutions on a UV–vis spectrophotometer (Lambda-35). The X-ray photoelectron spectroscopy (XPS) was characterized by using a spectrometer (Escalab 250Xi) with Al Kα X-ray radiation.

2.4. Electrochemical measurements

All solid materials including sulfur, TiO$_2$/GA composites and Ketjenblack (KB) carbon powders were dried at 50 °C in vacuum oven overnight before use. The cathodes for Li–S batteries were prepared by mixing 60 wt% of sulfur, 20 wt% of the TiO$_2$/GA composites, and 20 wt% of KB carbon in N-methyl-2-pyrrolidone (NMP) to form a slurry. The homogeneous slurry was then cast on one side of glass fiber and dried under vacuum at 50 °C for 12 h to evaporate the solvent [38]. The electrodes were cut into small round disks with a diameter of 12 mm afterwards. The CR2025 coin cells were assembled in an argon-filled glove box (<1 ppm of H$_2$O and O$_2$, Mikrouna). Li foil was the anode. Celgard 2325 membrane was used as the separator to isolate electrons. The electrolyte is 1,3-dioxolane (DOL) and 1,2-dimethoxymethane (DME) (1:1, v/v) with 1 M LiNO$_3$ additive. The galvanostatic charge-discharge experiments of the coin cells were obtained at different current densities between 1.7 and 2.7 V vs. Li/Li$^+$ by using a NEWARE cell test system (Shenzhen, China). Cyclic voltammetry (CV) tests were performed by electrochemical workstation (Arbin Instruments, USA) at a scan rate of 0.1 mV s^{-1}. Electrochemical impedance spectra (EIS) measurements were performed in the frequency range of 10 mHz–100 kHz at potentiostatic signal amplitudes of 5 mV.

3. Results and discussion

3.1. Preparation and structural analysis of TiO$_2$/GA composites

As illustrated in Fig. 1a, the overall synthetic procedure of the TiO$_2$/GA composites involves a simple one-pot hydrothermal and freeze-drying step. The hydrothermal method was used to prevent the aggregation of GO during reaction and obtain product with a
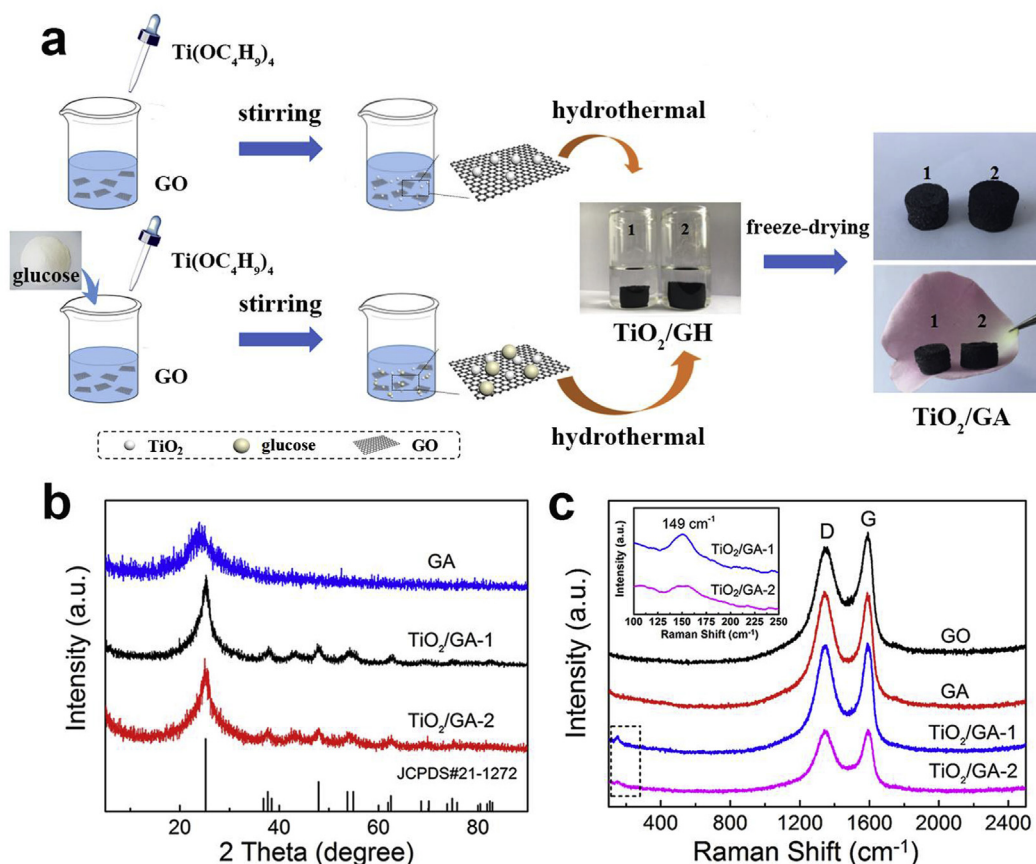
Fig. 1. (a) The schematic diagram of one-pot synthesis of the TiO$_2$/GA composites. (b) XRD patterns of GA, TiO$_2$/GA-1 and TiO$_2$/GA-2 composites. (c) Raman spectra of GO, GA, TiO$_2$/GA-1 and TiO$_2$/GA-2 composites.

large surface area and open framework. Two samples of TiO$_2$/GA-1 and TiO$_2$/GA-2 were synthesized. The difference is a certain amount of glucose was added into the precursor as a crosslinker and dispersing agent for the preparation of TiO$_2$/GA-2. After hydrothermal reaction at 180 °C for 12 h, it shows that both of the as-prepared TiO$_2$/graphene hydrogels (TiO$_2$/GH-1 and TiO$_2$/GH-2) are cylindrical shape. Notably, the TiO$_2$/GH-2 shows an obvious larger volume than TiO$_2$/GH-1. Freeze-drying of the hydrogels can avoid substantial reaggregation of graphene to get the good shape kept aerogels, which can be withstood on a flake of flower, indicating the lightweight characteristic.

The crystal structure of the TiO$_2$/GA-1 and TiO$_2$/GA-2 composites were investigated by XRD. For a control experiment, pure graphene aerogel (GA) was also prepared. After hydrothermal reaction, the (001) diffraction peaks (2θ = 10°) of GO does not appear in the GA sample (Fig. S1), indicating GO was reduced to graphene. The GA shows a strong diffraction peak at 2θ = 24° due to the re-aggregation and stack of the graphene sheets [39]. No obvious difference is observed for the XRD patterns of TiO$_2$/GA-1 and TiO$_2$/GA-2 composites. As is shown in Fig. 1b, the broad peaks at 2θ = 24° reveals the existence of graphene. The other peaks are in accordance with the anatase phase of TiO$_2$ standard spectrum (JCPDS No.21—1272). The sharp peak at 2θ = 25.3° is typical for anatase TiO$_2$, corresponding to its (101) facet [40,41]. The Raman spectra for all the samples in Fig. 1c present two typical peaks at 1350 and 1590 cm^{-1} attributed to the D and G bands, where D band is linked with the vibrations of the crystal border and G band represents the perfect sp^2 vibrations of graphitic crystal. The intensity ratio of D to G band has increased from 0.905 of GO to 1.012 of GA, 1.004 of TiO$_2$/

GA-1 and 1.006 of TiO$_2$/GA-2, proving that GO has been reduced successfully in the aerogels [39,42]. For TiO$_2$/GA-1 and TiO$_2$/GA-2 composites, the weak Raman shift band at 149 cm^{-1} relates to a typical characteristic feature of anatase TiO$_2$ [43].

The morphology and microstructure of the as-prepared 3D TiO$_2$/GA networks were initially observed by FE-SEM. As can be seen in Fig. 2a—d, the interconnected 3D porous network with open pores from several hundred nanometers to tens of micrometers are visible for both of TiO$_2$/GA-1 and TiO$_2$/GA-2 composites. Interestingly, TiO$_2$/GA-2 composite possesses more well-defined porous structure within the ultrathin layer of aerogel matrix. In the composites, the contents of TiO$_2$ in TiO$_2$/GA-1 and TiO$_2$/GA-2 are 15.3 and 12.8 wt%, respectively, as calculated by TG analysis (Fig. 2e) [44]. An initial decrease in weight ca. 3% at around 100 °C corresponding to the evaporation of free water is noticed from the TG analysis. The trace of water may result from the remained water during freeze-drying or the absorbed moisture from air. However, there are no obvious TiO$_2$ particles or aggregations observed in the FE-SEM images. To further explore the porous structure and specific surface area of the TiO$_2$/GA composites, N$_2$ adsorption-desorption isotherms and the pore size distribution analysis were carried out. The N$_2$ adsorption/desorption plots (Fig. 2f) suggest a dramatically increased surface area of TiO$_2$/GA-2 compared with TiO$_2$/GA-1. The BET surface area is calculated to be 35.9 m^2 g^{-1} for TiO$_2$/GA-1, which is much lower than that of 192.7 m^2 g^{-1} for TiO$_2$/GA-2. In addition, the volumes of micropores smaller than 2 nm and mesopores mainly fell in the range of 2—15 nm of TiO$_2$/GA-2 are increased significantly (Fig. 2g) [45]. The results indicate the addition of glucose into the precursor has a significant effect on the
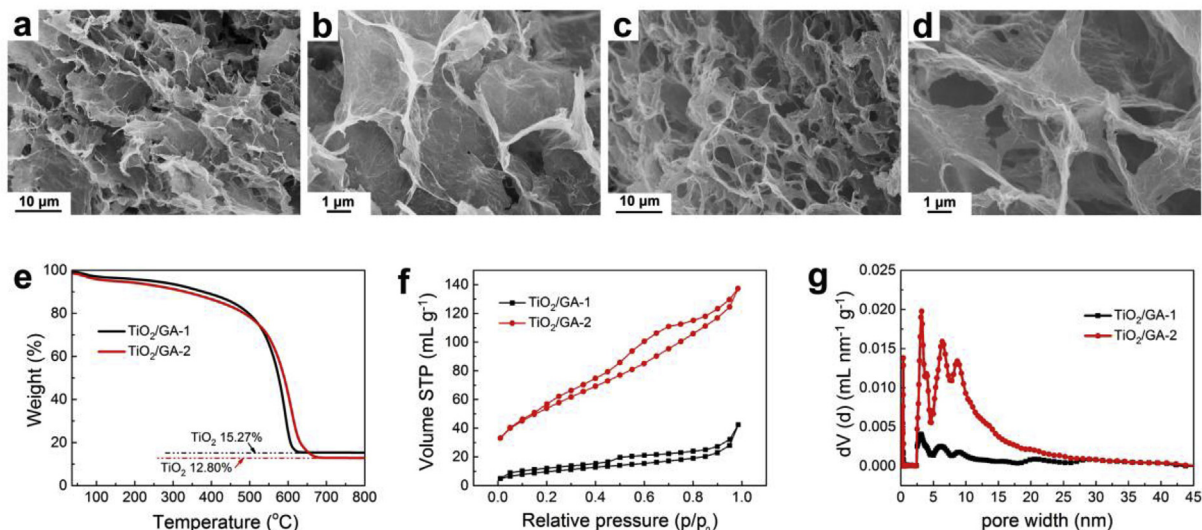
Fig. 2. SEM images of (a, b) TiO_2/GA-1, (c, d) TiO_2/GA-2 composites at low and high magnifications. (e) TG curves of TiO_2/GA-1 and TiO_2/GA-2 composites under air atmosphere with a heating rate of 20 °C min^{-1}. (f, g) N_2 adsorption-desorption isotherms and pore size distribution of TiO_2/GA-1 and TiO_2/GA-2 composites.

structure of aerogel products. SEM images of pure glucose show that nano-sized spherical carbon was formed after hydrothemal reaction at 180 °C for 12 h (Fig. S2). It could be speculated that glucose may be transformed into oligosaccharide and aromatic compounds after dehydration reaction. Then the molecules of oligosaccharide were crosslinked at a high temperature, after nucleation and growth, forming spherical carbon with functional groups. This spherical carbon might be interconnected with graphene sheets, to some extent, playing a part in increasing the pores of the aerogel by cooperative dispersion, so that the porosity of the aerogel became larger [46].

High-resolution TEM images reveal that the ultrafine TiO_2 nanoparticles with diameters of 5–10 nm were uniformly dispersed on the graphene nanosheets of TiO_2/GA-1 (Fig. 3a–c) and TiO_2/GA-2 (Fig. 3d–f). Especially, the distinct interplanar spacing of TiO_2 nanoparticles is 0.35 nm, corresponding to the lattice spacing of (101) plane of anatase TiO_2 [47]. Such a unique structure of the interconnected 3D graphene networks is strongly dependent on the ratios of TiO_2 and graphene. For example, other three TiO_2/GA composites with different TiO_2 contents of 3.5, 54.6 and 75.2 wt% (see TG curves in Fig. S3), respectively, are prepared by adjusting the concentration of $Ti(OC_4H_9)_4$ in ethanol solutions but without addition of glucose in the precursors. These three samples are

marked as TiO_2/GA-3%, TiO_2/GA-55% and TiO_2/GA-75%, respectively. SEM images of the TiO_2/GA with 3.5 wt% TiO_2 display the similar morphology to TiO_2/GA-1 without visible TiO_2 particles (Fig. S4a–c). The higher ratios of TiO_2 always result in the formation of aggregated TiO_2 particles (Fig. S4d–f) or bulks (Fig. S4g–i) onto the nanosheets of graphene, leading to collapse of graphene networks.

3.2. Interactions between Li_2S_n and TiO_2/GA composites

To verify the interactions between soluble Li_2S_n and TiO_2/GA composites, the adsorption experiment was conducted as demonstrated in Fig. 4a. For a control experiment, pure anatase TiO_2 with a particle size of 25–50 nm was synthesized via hydrothermal reaction (Fig. S5a–d). The phase purity of the obtained TiO_2 was confirmed by XRD (JCPDS No.21–1272) (Fig. S5e). For distinguishing different samples, 3 mL of 8 mM Li_2S_6 was used as the reference solution (sample 1#). 10 mg GA, TiO_2/GA-1 composite, TiO_2/GA-2 composite or pure TiO_2 was added into the same Li_2S_6 solution, which was marked as sample 2#, 3#, 4# and 5#, respectively. The solution colour of 5# by adding pure TiO_2 changed from dark-brown to yellow immediately, indicating strong interactions between lithium polysulfides and TiO_2 nanoparticles [29,48]. The
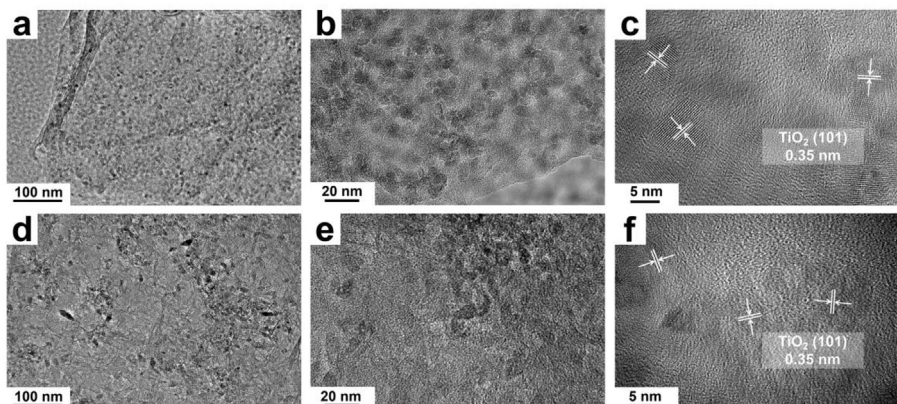
Fig. 3. TEM images of (a–c) TiO_2/GA-1 and (d–f) TiO_2/GA-2 composites at low and high magnifications.
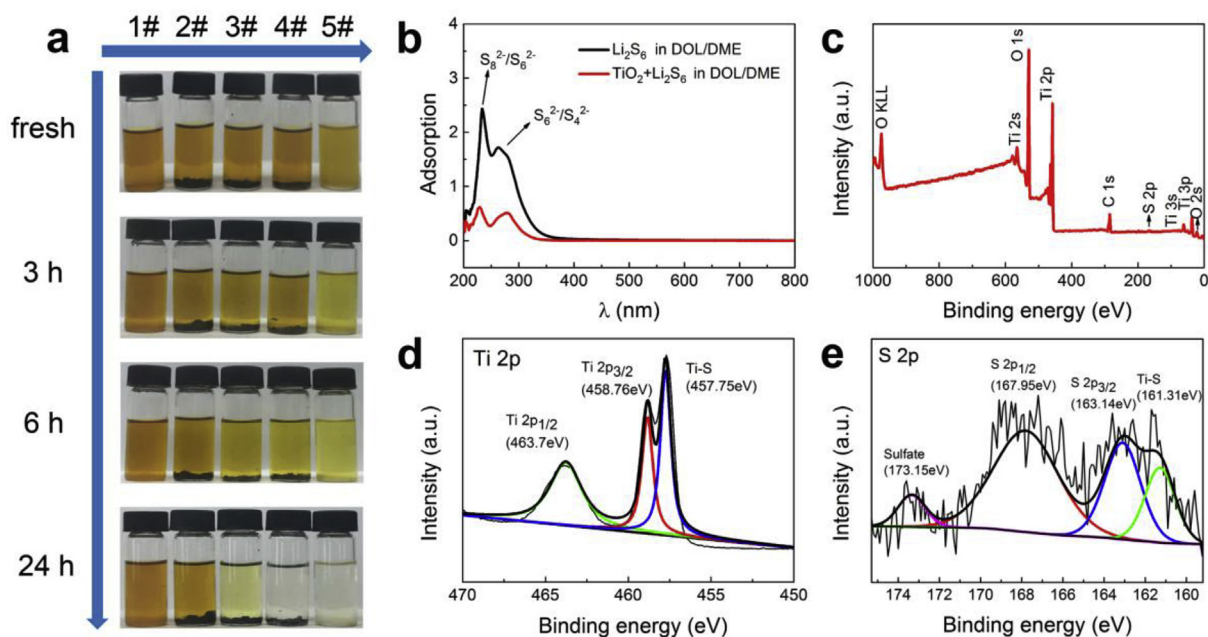
Fig. 4. (a) Optical photographs of the adsorption of 8 mM Li_2S_6 solution (1#) with 10 mg GA (2#), TiO_2/GA-1 composite (3#), TiO_2/GA-2 composite (4#) and pure TiO_2 (5#) added. (b) UV/vis spectra of Li_2S_6 solution in DOL/DME with and without pure TiO_2. (c–e) XPS spectra of pure TiO_2 after adsorption of Li_2S_6 solution: wide spectrum, high-resolution spectra of Ti 2p and S 2p.

colour of 2# by adding GA changed very slightly even after standing for 6 h. In contrast, all others show obvious colour change to light yellow. After standing for 24 h, the solution containing TiO_2/GA-2 and pure TiO_2 turned completely transparent, while the solution containing TiO_2/GA-1 was still slightly coloured. Compared to TiO_2/GA-1, the TiO_2/GA-2 composite exhibits reinforced adsorbability, as expected from its higher surface area and porosity. UV−vis absorption spectra of the transparent solution of 5# exhibits a decreased peak intensity than the reference solution (Fig. 4b), confirming the TiO_2 nanoparticles effectively adsorbed the lithium polysulfide [47]. The sharp peak located at 225 nm is attributed to S_8^{2-} or S_6^{2-} species, and the shoulder peak at 280 nm is attributed to S_6^{2-} or S_4^{2-} species [49].

XPS analysis was performed in order to examine the types of interactions between TiO_2 and Li_2S_6. The high-resolution XPS spectra of Li_2S_6-adsorbed TiO_2 nanoparticles is demonstrated in Fig. 4c. The obvious signals of Ti, O, and weak signal of S further reveal the successful introduction of sulfur into the TiO_2 [50]. The Ti 2p spectra in Fig. 4d shows two sharp peaks appeared at 458.76 and 463.72eV, corresponding to the core levels of Ti $2p_{1/2}$ and Ti $2p_{3/2}$ of Ti^{4+} in TiO_2, respectively. Besides, the peak at 457.75 eV can be ascribed to the Ti−S bond in titanium oxysulfide (TiOS) phase, indicating the presence of Ti−S interaction after adsorption by polysulfide. Fig. 4e shows two prominent S 2p peaks centered at 167.95 and 163.14 eV, which are assigned to S $2p_{1/2}$ and S $2p_{3/2}$ spin-orbit doublets of bridging sulfur and terminal sulfur, respectively. The peak at 173.15 eV is related to the presence of sulfate. Moreover, the S $2p_{3/2}$ peak at 161.31 eV is assigned to Ti−S bond in TiOS, further confirming the Ti−S interaction. As depicted in the XPS results, Ti−S bonding and sulfate contribute largely to the strong chemical interaction of TiO_2 towards polysulfides [43,51,52].

3.3. Electrochemical performance of TiO_2/GA composites

All materials were dried thoroughly under vacuum before fabrication of electrodes. FT-IR measurements on the TiO_2/GA-1 and TiO_2/GA-2 composites could exclude the presence of any

remained water (Fig. S6). To get an insight into the electrochemical performance of the as-prepared TiO_2/GA composites applied as supporting 3D networks for sulfur cathode (marked as S@TiO_2/GA), typical CV curves at a scan rate of 0.1 mV s^{-1} within the potential range of 1.7−2.7 V are presented in Fig. 5a and d. To confirm that the TiO_2 nanoparticles are electrochemically inactive in the potential range, the CV of the TiO_2 electrode was examined as well, and the result is shown in Fig. S7. Both the CV curves of S@TiO_2/GA-1 (Fig. 5a) and S@TiO_2/GA-2 (Fig. 5d) exhibit typical redox peaks of sulfur. The two typical cathodic peaks at around 2.25 V and 1.98 V correspond to the reduction of S_8 to long-chain Li_2S_n and their further reduction to short-chain insoluble Li_2S. The anodic peak at around 2.4 V is related to the reversible oxidation from Li_2S to S_8. In contrast, the CV curve of TiO_2 electrode without sulfur shows a small oxidation peak that appeared at 1.95 V (Fig. S7). The peak cannot be observed in the CV curves of S@TiO_2/GA composites due to the low content of TiO_2 [44].

The galvanostatic cyclic test of the electrodes was performed within a potential window of 1.7−2.7 V. The representative charge–discharge profiles of S@TiO_2/GA-1 (Fig. 5b) and S@TiO_2/GA-2 (Fig. 5e), recorded from 0.2 C (1 C = 1675 mA g^{-1}) to 2 C at the 10th cycle, display two pairs of charge−discharge plateaus with respect to the Li−S redox reactions. At 0.2, 0.5, 1, and 2 C, the S@TiO_2/GA-2 cathode delivers a discharge capacity of 987, 948, 844 and 931 mAh g^{-1}, respectively. Whereas a relatively lower specific capacity of 931, 869, 817 and 762 mAh g^{-1} is displayed by S@TiO_2/GA-1 cathode. The higher utilization of sulfur in S@TiO_2/GA-2 should be owing to the greatly reduced resistance of electron and ion transport in the highly porous 3D interconnected conductive matrix, resulting from the increased surface area and more well-defined porous structure by addition of glucose to the precursors. In addition, the EIS analysis demonstrated in Fig. S8 provides compelling evidence of the decreased interfacial resistance of the cell with S@TiO_2/GA-2 composite. The S@TiO_2/GA-2 cathode holds a discharge capacity of 553 mAh g^{-1} after 500 cycles at 0.2 C, which is higher than that of 480 mAh g^{-1} for the S@TiO_2/GA-1 cathode (Fig. 5c, f). The capacity retention of S@TiO_2/GA-2 increases at a
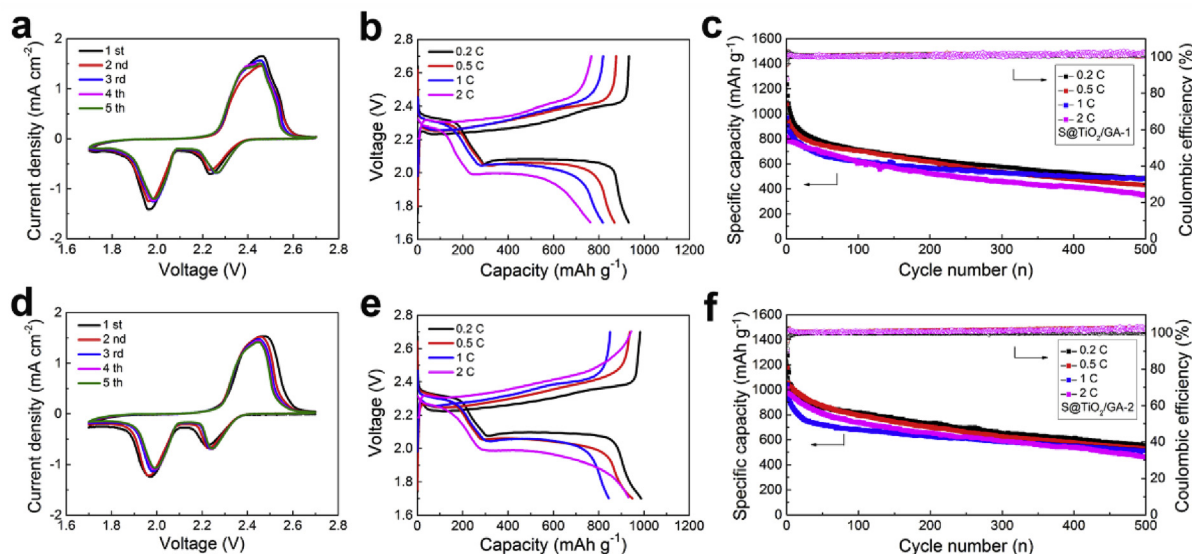
Fig. 5. (a, d) CV curves of S@TiO$_2$/GA-1 and S@TiO$_2$/GA-2 electrodes at 0.1 mV s^{-1} (b, e) Galvanostatic charge–discharge profiles of S@TiO$_2$/GA-1 and S@TiO$_2$/GA-2 electrodes at the 10th cycle. (c, f) Cyclic performance and coulombic efficiency profiles of S@TiO$_2$/GA-1 and S@TiO$_2$/GA-2 electrodes at 0.2, 0.5, 1, and 2 C over 500 cycles.

moderate current rate, reaching 512 mAh g^{-1} after 500 cycles at 1 C, indicating 60% retention after 500 cycles with respect to the capacity after the 10th cycle. The coulombic efficiency stabilized at around 100% further confirms the effectively suppressed dissolution and diffusion of soluble polysulfides. A comparison of the electrochemical performance between this work and the previously reported sulfur cathodes based on TiO$_2$ or other metal oxides, is shown in Table S1. In a careful review of previous reports, it can be seen that the strategy and focus of this work are essentially different from previous ones involving use of TiO$_2$, graphene and sulfur [43,44,53–56]. The synthetic routes have great effect on morphological structures of final products, resulting in varied cell performance. For example, Li et al. introduced a solution route to prepare a sulfur@TiO$_2$@reduced graphene oxide (S@TiO$_2$@rGO) composite, in which sulfur nanoparticles were wrapped by delaminated TiO$_2$ nanosheets and rGO matrix was employed to wrap around the S@TiO$_2$ [53]. Song et al. reported a tubular TiO$_2$/rGO composite as a sulfur host [55]. Raw materials of TiO$_2$ and GO powders were dispersed in a highly concentrated alkali solvent. After a hydrothermal synthesis, the reaction product was treated in acid solution and heating in N$_2$ flow, leading to TiO$_2$ nanotubes wrapped by rGO sheets. In terms of our work, two unique insights are achieved through the rational design of TiO$_2$/GA composites: (i) The structure of the interconnected 3D porous network is strongly dependent on the ratios of TiO$_2$ and graphene, which have largely been ignored previously. (ii) The surface area and pore size contribution can be adjusted simply by adding glucose as a crosslinker and dispersing agent, leading to enhanced adsorption of soluble Li$_2$S$_n$. Therefore, the current S@TiO$_2$/GA-2 electrode presents high specific capacity, decent cyclic efficiencies and rate capability.

In addition, we evaluated the cell performance of other more electrodes built on S@GA and S@TiO$_2$/GA composites with different TiO$_2$ contents of 3.5, 54.6 and 75.2 wt% (it should be noted that the TiO$_2$ content is calculated based on the weight of TiO$_2$/GA). The sulfur content is 60 wt% in all the electrodes. Compared with the S@GA electrode (Fig. S9a), improved cyclic performance is obtained even when the content of TiO$_2$ in the TiO$_2$/GA is as low as 3.5 wt% (Fig. S9b). By increasing the TiO$_2$ content to 54.6 wt%, the capacity decays rapidly at increased current rates (Fig. S9c). No more than

200 mAh g^{-1} of specific capacity can be kept after 500 cycles at 1 C. As the TiO$_2$ amount increases as high as 75.2 wt%, the cyclic stability deteriorates more obviously after 300 cycles at the current densities higher than 0.5 C (Fig. S9d). These results suggest the overall cell performance of Li–S battery depends strongly on the structure of electrode. An excessive TiO$_2$ would not only destroy the porous 3D interconnected networks of aerogel, but also ruin the performance of the batteries. To further confirm the effectiveness of glucose, we added 20 mg glucose into the precursor of TiO$_2$/GA-3% composite and prepared its counterpart, named TiO$_2$/GA-3%-2 composite. The final content of TiO$_2$ in the two samples are 3.5 and 3.3 wt%, respectively, with the negligible difference. From the long-term cyclic performance over 500 cycles at a moderate current rate of 0.5 C (Fig. S10), it can be seen that S@TiO$_2$/GA-3%-2 composite exhibits a higher specific capacity and cyclic stability than that of S@TiO$_2$/GA-3%. However, the extremely low content of TiO$_2$ is insufficient to confine polysulfides. After 500 cycles, the specific capacity maintained for S@TiO$_2$/GA-3%-2 is about 500 mAh g^{-1}, which is lower than the 530 mAh g^{-1} of S@TiO$_2$/GA-2. Therefore, it is crucial to adjust the content of TiO$_2$ in the graphene aerogels for the rational design of cathode materials for Li–S batteries.

4. Conclusions

In summary, we have fabricated a lightweight 3D TiO$_2$/GA with hierarchical pores for the sulfur cathode of Li–S batteries by a one-pot chemical synthesis process. In this rational design, TiO$_2$ plays an essential role in improving the capacity and coulombic efficiency by chemically adsorbed the soluble polysulfides. The porous graphene aerogel affords an additional electronic conductive network, which facilitates the rapid mass transportation. Moreover, the sulfur cathode built on the TiO$_2$/GA-2 composite by adding glucose as a crosslinker and dispersing agent exhibits a larger surface area and multiple pore size distribution, leading to a higher specific capacity, superior rate capability and ultra-long cyclic performance. Various TiO$_2$/GA composites with different contents of TiO$_2$ are synthesized, while the one containing 15.3 wt% TiO$_2$ demonstrates the best electrochemical performance. The new design is expected to have great potential on the development of high performance Li–S batteries.

Acknowledgements

Appendix A. Supplementary data

Supplementary data to this article can be found online at https://doi.org/10.1016/j.electacta.2018.09.109.

References

[1] M. Armand, J.M. Tarascon, Nature 451 (2008) 652—657.
[2] P.G. Bruce, S.A. Freunberger, L.J. Hardwick, J.M. Tarascon, Nat. Mater. 11 (2011) 19—29.
[3] H.B. Lin, J.N. Hu, H.B. Rong, Y.M. Zhang, S.W. Mai, L.D. Xing, M.Q. Xu, X.P. Li, W.S. Li, J. Mater. Chem. A 2 (2014) 9272—9279.
[4] S. Evers, L.F. Nazar, Acc. Chem. Res. 46 (2012) 1135—1143.
[5] Z. Gao, Y. Zhang, N. Song, X. Li, Electrochim. Acta 246 (2017) 507—516.
[6] J. Liu, W. Li, L. Duan, X. Li, L. Ji, Z. Geng, K. Huang, L. Lu, L. Zhou, Z. Liu, W. Chen, L. Liu, S. Feng, Y. Zhang, Nano Lett. 15 (2015) 5137—5142.
[7] L.-N. Wang, J.-Y. Liu, S.Y. Yuan, Y.Y. Wang, Y.Y. Xia, Energy Environ. Sci. 9 (2016) 224—231.
[8] A. Vizintin, L. Chabanne, E. Tchernychova, I. Arcon, L. Stievano, G. Aquilanti, M. Antonietti, T.-P. Fellinger, R. Dominko, J. Power Sources 344 (2017) 208—217.
[9] R. Fang, S. Zhao, P. Hou, M. Cheng, S. Wang, H.M. Cheng, C. Liu, F. Li, Adv. Mater. 28 (2016) 3374—3382.
[10] X. Fang, W. Weng, J. Ren, H. Peng, Adv. Mater. 28 (2016) 491—496.
[11] G. Zhou, L. Li, C. Ma, S. Wang, Y. Shi, N. Koratkar, W. Ren, F. Li, H.-M. Cheng, Nano Energy 11 (2015) 356—365.
[12] J. Zhou, N. Lin, W. Cai, C. Guo, K. Zhang, J. Zhou, Y. Zhu, Y. Qian, Electrochim. Acta 218 (2016) 243—251.
[13] J. Zhang, C.-P. Yang, Y.-X. Yin, L.-J. Wan, Y.-G. Guo, Adv. Mater. 28 (2016) 9539—9544.
[14] Q. Zhu, Q. Zhao, Y. An, B. Anasori, H. Wang, B. Xu, Nano Energy 33 (2017) 402—409.
[15] C. Zhang, H.B. Wu, C. Yuan, Z. Guo, X.W. Lou, Angew. Chem. Int. Ed. 51 (2012) 9592—9595.
[16] J.S. Lee, W. Kim, J. Jang, A. Manthiram, Adv. Energy Mater. 7 (2017) 1601943.
[17] X. Yang, W. Zhu, G. Cao, X. Zhao, RSC Adv. 6 (2016) 7159—7171.
[18] M.D. Patel, E. Cha, C. Kang, B. Gwalani, W. Choi, Carbon 118 (2017) 120—126.
[19] R. Fang, G. Li, S. Zhao, L. Yin, K. Du, P. Hou, S. Wang, H.-M. Cheng, C. Liu, F. Li, Nano Energy 42 (2017) 205—214.
[20] Z. Zhang, L.-L. Kong, S. Liu, G.-R. Li, X.-P. Gao, Adv. Energy Mater. 7 (2017), 1602543.
[21] O. Ogoke, G. Wu, X. Wang, A. Casimir, L. Ma, T. Wu, J. Lu, J. Mater. Chem. A 5 (2017) 448—469.
[22] W. Kang, N. Deng, J. Ju, Q. Li, D. Wu, X. Ma, L. Li, M. Naebe, B. Cheng, Nanoscale 8 (2016) 16541—16588.
[23] Y. Pang, Y. Wen, W. Li, Y. Sun, T. Zhu, Y. Wang, Y. Xia, J. Mater. Chem. A 5 (2017) 17926—17932.
[24] Z. Li, J. Zhang, X.W. Lou, Angew. Chem. Int. Ed. 54 (2015) 12886—12890.
[25] X. Liang, L.F. Nazar, ACS Nano 10 (2016) 4192—4198.
[26] Z. Cui, C. Zu, W. Zhou, A. Manthiram, J.B. Goodenough, Adv. Mater. 28 (2016) 6926—6931.
[27] M. Yu, J. Ma, H. Song, A. Wang, F. Tian, Y. Wang, H. Qiu, R. Wang, Energy Environ. Sci. 9 (2016) 1495—1503.
[28] Z. Xiao, Z. Yang, L. Wang, H. Nie, M. Zhong, Q. Lai, X. Xu, L. Zhang, S. Huang, Adv. Mater. 27 (2015) 2891—2898.
[29] F. Liu, Q. Xiao, H.B. Wu, F. Sun, X. Liu, F. Li, Z. Le, L. Shen, G. Wang, M. Cai, Y. Lu, ACS Nano 11 (2017) 2697—2705.
[30] W. Li, J. Hicks-Garner, J. Wang, J. Liu, A.F. Gross, E. Sherman, J. Graetz, J.J. Vajo, P. Liu, Chem. Mater. 26 (2014) 3403—3410.
[31] X. Liu, J.Q. Huang, Q. Zhang, L. Mai, Adv. Mater. 29 (2017), 1601759.
[32] T. Zhou, W. Lv, J. Li, G. Zhou, Y. Zhao, S. Fan, B. Liu, B. Li, F. Kang, Q.-H. Yang, Energy Environ. Sci. 10 (2017) 1694—1703.
[33] Z. Li, J. Zhang, B. Guan, D. Wang, L.M. Liu, X.W. Lou, Nat. Commun. 7 (2016) 13065.
[34] L. Yang, G. Li, X. Jiang, T. Zhang, H. Lin, J.Y. Lee, J. Mater. Chem. A 5 (2017) 12506—12512.
[35] Z. Wei Seh, W. Li, J.J. Cha, G. Zheng, Y. Yang, M.T. McDowell, P.C. Hsu, Y. Cui, Nat. Commun. 4 (2013) 1331.
[36] Z. Zhang, Z. Li, F. Hao, X. Wang, Q. Li, Y. Qi, R. Fan, L. Yin, Adv. Funct. Mater. 24 (2014) 2500—2509.
[37] Z. Gao, J. Yang, J. Huang, C. Xiong, Q. Yang, Nanoscale 9 (2017) 17710—17716.
[38] L.N. Wang, J.Y. Liu, S. Haller, Y.Y. Wang, Y.Y. Xia, Chem. Commun. 51 (2015) 6996—6999.
[39] S. Stankovich, D.A. Dikin, R.D. Piner, K.A. Kohlhaas, A. Kleinhammes, Y. Jia, Y. Wu, S.T. Nguyen, R.S. Ruoff, Carbon 45 (2007) 1558—1565.
[40] Z. Yang, D. Choi, S. Kerisit, K.M. Rosso, D. Wang, J. Zhang, G. Graff, J. Liu, J. Power Sources 192 (2009) 588—598.
[41] S. Evers, T. Yim, L.F. Nazar, J. Phys. Chem. C 116 (2012) 19653—19658.
[42] Y. Zhu, S. Murali, W. Cai, X. Li, J.W. Suk, J.R. Potts, R.S. Ruoff, Adv. Mater. 22 (2010) 3906—3924.
[43] Y. Li, Q. Cai, L. Wang, Q. Li, X. Peng, B. Gao, K. Huo, P.K. Chu, ACS Appl. Mater. Interfaces 8 (2016) 23784—23792.
[44] J.Q. Huang, Z. Wang, Z.L. Xu, W.G. Chong, X. Qin, X. Wang, J.K. Kim, ACS Appl. Mater. Interfaces 8 (2016) 28663—28670.
[45] J. He, Y. Chen, P. Li, F. Fu, Z. Wang, W. Zhang, J. Mater. Chem. A 3 (2015) 18605—18610.
[46] H. Ge, T. Hao, H. Osgood, B. Zhang, L. Chen, L. Cui, X.M. Song, O. Ogoke, G. Wu, ACS Appl. Mater. Interfaces 8 (2016) 9162—9169.
[47] B. Qiu, M. Xing, J. Zhang, J. Am. Chem. Soc. 136 (2014) 5852—5855.
[48] S.H. Chung, A. Manthiram, Chem. Commun. 50 (2014) 4184—4187.
[49] Z. Xiao, Z. Yang, L. Wang, H. Nie, M. Zhong, Q. Lai, X. Xu, L. Zhang, S. Huang, Adv. Mater. 27 (2015) 2891—2898.
[50] T. Lei, Y. Xie, X. Wang, S. Miao, J. Xiong, C. Yan, Small 13 (2017) 1701013.
[51] X. Song, T. Gao, S. Wang, Y. Bao, G. Chen, L.-X. Ding, H. Wang, J. Power Sources 356 (2017) 172—180.
[52] C. Yuan, S. Zhu, H. Cao, L. Hou, J. Lin, Nanotechnology 27 (2016), 045403.
[53] J. Li, M. Zhu, P. Hu, X. Wang, L. Zhang, M. Li, Eur. J. Inorg. Chem. 26 (2017) 3248—3252.
[54] X. Shang, P. Guo, T. Qin, M. Liu, M. Lv, D. Liu, D. He, Adv. Mater. Interfaces 5 (2018) 1701602.
[55] J. Song, J. Zheng, S. Feng, C. Zhu, S. Fu, W. Zhao, D. Du, Y. Lin, Carbon 128 (2018) 63—69.
[56] M. Yu, J. Ma, H. Song, A. Wang, F. Tian, Y. Wang, H. Qiu, R. Wang, Energy Environ. Sci. 9 (2016) 1495—1503.